

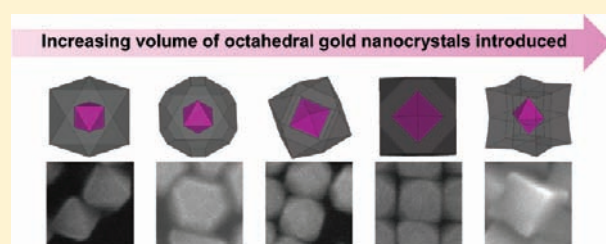
Fabrication of Au–Pd Core–Shell Heterostructures with Systematic Shape Evolution Using Octahedral Nanocrystal Cores and Their Catalytic Activity

Chih-Wen Yang, Kaushik Chanda, Po-Heng Lin, Yu-Ning Wang, Ching-Wen Liao, and Michael H. Huang*

Department of Chemistry, National Tsing Hua University, Hsinchu 30013, Taiwan

S Supporting Information

ABSTRACT: By using octahedral gold nanocrystals with sizes of approximately 50 nm as the structure-directing cores for the overgrowth of Pd shells, Au–Pd core–shell heterostructures with systematic shape evolution can be directly synthesized. Core–shell octahedra, truncated octahedra, cuboctahedra, truncated cubes, and concave cubes were produced by progressively decreasing the amount of the gold nanocrystal solution introduced into the reaction mixture containing cetyltrimethylammonium bromide (CTAB), H_2PdCl_4 , and ascorbic acid. The core–shell structure and composition of these nanocrystals has been confirmed. Only the concave cubes are bounded by a variety of high-index facets. This may be a manifestation of the release of lattice strain with their thick shells at the corners. Formation of the $[\text{CTA}]_2[\text{PdBr}_4]$ complex species has been identified spectroscopically. Time-dependent UV–vis absorption spectra showed faster Pd source consumption rates in the growth of truncated cubes and concave cubes, while a much slower reduction rate was observed in the generation of octahedra. The concave cubes and octahedra were used as catalysts for a Suzuki coupling reaction. They can all serve as effective and recyclable catalysts, but the concave cubes gave higher product yields with a shorter reaction time attributed to their high-index surface facets. The concave cubes can also catalyze a wide range of Suzuki coupling reactions using aryl iodides and arylboronic acids with electron-donating and -withdrawing substituents.



INTRODUCTION

A recent development in the synthesis of inorganic nanocrystals is aimed at the fabrication of core–shell heterostructures with both polyhedral cores and shells. This type of heterostructure is interesting not only because it can present significant synthetic challenges, but the resulting nanostructures may also exhibit enhanced physical and chemical properties resulting from the shell surface control and the encapsulated core materials.^{1–16} Most of these core–shell nanostructures are bimetallic systems. Recently, Au– Cu_2O core–shell heterostructures with systematic shape evolution from cubic to octahedral structures have been generated using a variety of polyhedral gold nanocrystal cores including octahedra and rhombic dodecahedra.^{17,18} Highly facet-dependent electrical conductivity behavior and photocatalytic activity of these metal–semiconductor core–shell heterostructures have been demonstrated.^{18,19} Despite some success in the preparation of these heterostructures, a report on the direct synthesis of bimetallic core–shell nanocrystals with systematic shell morphology evolution using the same polyhedral cores is still not available. Yang et al. have used cubic Pt seeds for the overgrowth of Pd shells to form Pt–Pd core–shell cubes.³ To alter the shell morphology to cuboctahedral and octahedral structures, different amounts of NO_2 need to be added to react with the preformed core–shell cubes. This procedure is not so convenient. Thus, it is desirable to develop a simple approach to

achieve such shape evolution of shells. For Au–Pd core–shell heterostructures, the task can become more difficult due to their substantial lattice mismatch of $\sim 4.6\%$.¹

Here, we report octahedral gold nanocrystal-directed overgrowth of Au–Pd core–shell heterostructures with fine control of particle shapes from octahedral to truncated octahedral, cuboctahedral, truncated cubic, and concave cubic structures. Remarkably, the shell morphology can be tuned simply by varying the amount of the gold nanocrystal cores added to the reaction mixture. The core–shell particle structures have been extensively determined by several analytical techniques. Interestingly, the concave cubes possess several different high-index facets. UV–vis absorption spectra were taken to follow the growth rates of these heterostructures. Different growth rates have been found in the formation of different nanocrystal morphologies. A few Pd nanostructures such as nanorods, branched nanostructures, and Au@Pd tetrahedral (THH) nanocrystals have been examined for their use as catalysts for Suzuki coupling reactions.^{1,10} To assess the catalytic performance of the synthesized core–shell heterostructures, octahedra and concave cubes were chosen for their comparative catalytic activity. Both can serve as effective and recyclable catalysts for a

Received: September 28, 2011

Published: November 17, 2011

Suzuki–Miyaura coupling reaction. Concave cubes were found to be superior catalysts attributed to their possession of high-index surfaces.

EXPERIMENTAL SECTION

Chemicals. PdCl₂ powder (Aldrich, 99%), hydrogen tetrachloroaurate trihydrate (HAuCl₄·3H₂O, 99.9%, Aldrich), cetyltrimethylammonium chloride (CTAC, 95%, TCI), cetyltrimethylammonium bromide (CTAB, 98%, Alfa Aesar), sodium borohydride (NaBH₄, 98%, Aldrich), ascorbic acid (AA, 99.7%, Riedel de Haën), and potassium iodide (KI, J. T. Baker) were used as received. Commercially available reagents were used for the Suzuki coupling reactions.

Synthesis of Octahedral Gold Nanocrystal Cores. The procedure follows a seed-mediated synthesis approach developed in our laboratory.²⁰ A volume of 10 mL of aqueous solution containing 2.5×10^{-4} M HAuCl₄ and 0.1 M CTAC surfactant was prepared. Concurrently, 10 mL of 0.02 M ice-cold NaBH₄ solution was made. To the HAuCl₄ solution was added 0.45 mL of NaBH₄ solution with stirring. The resultant solution turned brown immediately, indicating the formation of gold seed particles with sizes of ~5 nm. A growth solution was prepared in each of two vials labeled A and B. First, 0.32 g of CTAC and 9.45 mL of deionized water were added to each vial. The vials were then kept in a water bath set at 30 °C. To both vials were added 250 μL of 0.01 M HAuCl₄ solution and 5 μL of 0.01 M KI solution. Finally, 220 μL of 0.04 M ascorbic acid was introduced. The total solution volume in each vial was 10 mL. The concentration of CTAC in the final solution was equal to 0.1 M. The solution color turned colorless. Next, 80 μL of the seed solution was added to the solution in vial A with shaking until the solution turned light pink. 80 μL of the solution in vial A then was transferred to vial B with thorough mixing for 10 s. Vial B was left undisturbed for 15 min for particle growth, and the solution was centrifuged at 6000 rpm for 10 min (Hermle Z323 centrifuge). The concentrated particles were dispersed in 1.5 mL of this solution.

Synthesis of Au–Pd Core–Shell Heterostructures. First, a 10 mM H₂PdCl₄ solution was prepared by completely dissolving 0.089 g of deep brown PdCl₂ powder in 25 mL of 50 mM HCl solution and diluting the solution to 50 mL using a volumetric flask. In a typical synthesis of Au–Pd core–shell octahedra, 7.8 mL of deionized water, 0.055 g of CTAB, and 0.45 mL of the octahedral Au nanocrystal solution were introduced into a sample vial. For the growth of Au–Pd core–shell truncated octahedra, cuboctahedra, truncated cubes, and concave cubes, 0.4, 0.35, 0.3, and 0.2 mL of the octahedral Au nanocrystal solution, and 7.85, 7.90, 7.95, and 8.05 mL of deionized water, were transferred, respectively. Different amounts of water were added to keep the final solution volume at 10 mL. The vial was kept in a water bath set at 35 °C. 0.75 mL of 0.01 M H₂PdCl₄ solution then was introduced into the vial. After the vial was stirred for 15 min, the solution turned orange. The color change is attributed to the formation of the [CTA]₂[PdBr₄] complex species. Next, 1 mL of 0.1 M ascorbic acid solution was added. CTAB concentration in the final solution was 1.5×10^{-2} mM. The reaction mixture was stirred for 12 h, and centrifuged at 4000 rpm for 10 min.

Time-Dependent UV–Vis Absorption Spectroscopic Measurements. The spectra were taken to evaluate the relative reaction rates in the synthesis of different heterostructures. The solution volume used here is twice that employed for the formation of core–shell nanocrystals. After ascorbic acid was added, 180 μL of the reaction mixture was removed and diluted with 400 μL of deionized water at different times for the UV–vis measurements. To monitor the formation of the [CTA]₂[PdBr₄] complex species, 0.0275 g of CTAB and 4.625 mL of water were mixed together. After 375 μL of 0.01 M H₂PdCl₄ solution was introduced, UV–vis absorption spectra were taken every 3 min.

Suzuki Coupling Reactions. Octahedral and concave cubic Au–Pd core–shell nanostructures were used as catalysts for the Suzuki–Miyaura cross-coupling reactions. For the synthesis of biphenyl, phenylboronic acid (0.0098 g, 0.08 mmol, 1.1 equiv) and potassium phosphate hydrate (0.030 g, 0.13 mmol, 1.6 equiv) were placed in a 25 mL round-bottomed flask containing 5 mL of water and ethanol in 4:1 volume ratio. After the mixture was stirred for 5 min for dissolution of phenylboronic acid, iodobenzene (0.015 g, 0.07 mmol, 1.0 equiv) was added into the solution. A fixed volume of colloidal solution of nanocrystals was immediately added (50 μL of Au–Pd octahedra with a calculated total particle surface area of 0.051 cm²/μL solution or 67 μL of Au–Pd concave cubes with a total particle surface area 0.037 cm²/μL solution; see the Supporting Information for details of calculations). Subsequently, the reaction mixture was heated to 80 °C with stirring. The progress of the reaction was monitored by thin-layer chromatography (TLC). After completion of the reaction, the solvent was removed under reduced pressure. The residue left was redissolved in 5 mL of ethyl acetate and washed with water. The combined organic layer was dried over anhydrous Na₂SO₄. The combined filtrate was subjected to evaporation to obtain the crude compound, which was purified over silica gel column (60–120 mesh) using hexane as eluent to provide the coupling product. To evaluate the extent of versatility of these nanocrystal catalysts, the same coupling reaction was repeated with different substituents on aryl iodides and phenylboronic acids containing electron-donating and electron-withdrawing groups. Concave cubes were chosen as the catalysts in these reactions.

In addition, the recyclability of the Au–Pd octahedra and concave cubes as catalysts was also surveyed. After completion of the reaction, the reaction mixture was diluted with 10 mL of ethyl acetate and washed with water. Au–Pd core–shell nanocrystals should stay in the aqueous phase. To the aqueous solution were added freshly measured quantities of phenylboronic acid and potassium phosphate hydrate. After the mixture was stirred for 5 min for dissolution of the phenylboronic acid, iodobenzene was added into the solution. Subsequently, the reaction mixtures were heated to 80 °C with stirring. The progress of the reaction was also monitored by TLC. The same process was repeated one more time.

Instrumentation. Scanning electron microscopy (SEM) images of the samples were acquired using a JEOL JSM-7000F electron microscope. Transmission electron microscopy (TEM) characterization was performed on a JEOL-2100 electron microscope with an operating voltage of 200 kV. Elemental mapping images were obtained using another JEOL-2100 electron microscope equipped with a scanning TEM unit and an Inca Energy 250 detector from Oxford Instruments. High-resolution TEM images were taken with the use of a JEOL JEM-3000F electron microscope. Powder X-ray diffraction (XRD) patterns were recorded on a Shimadzu XRD-6000 diffractometer with Cu K α radiation. UV–vis absorption spectra were taken using a JASCO V-570 spectrophotometer. ¹H NMR (400 or 600 MHz) and ¹³C NMR (100 or 150 MHz) were recorded with a Varian 400 or Bruker DRX600 spectrometer. Chemical shifts are reported in ppm relative to the internal solvent peak ($\delta = 7.26$ and 77.0 ppm, respectively, for CDCl₃). Coupling constants, *J*, are given in Hz. Multiplicities of peaks are given as d (doublet), m (multiplet), s (singlet), and t (triplet). TLC plates were Merck silica gel 60 F254 on aluminum. Flash column chromatography was performed with silica gel (60–100 mesh).

RESULTS AND DISCUSSION

In this study, octahedral gold nanocrystals were used as cores for the formation of Au–Pd core–shell heterostructures with systematic shape control. The gold nanocrystals were synthesized following a seed-mediated and iodide-assisted growth method.²⁰ Uniform gold octahedra with sizes of ~50 nm were

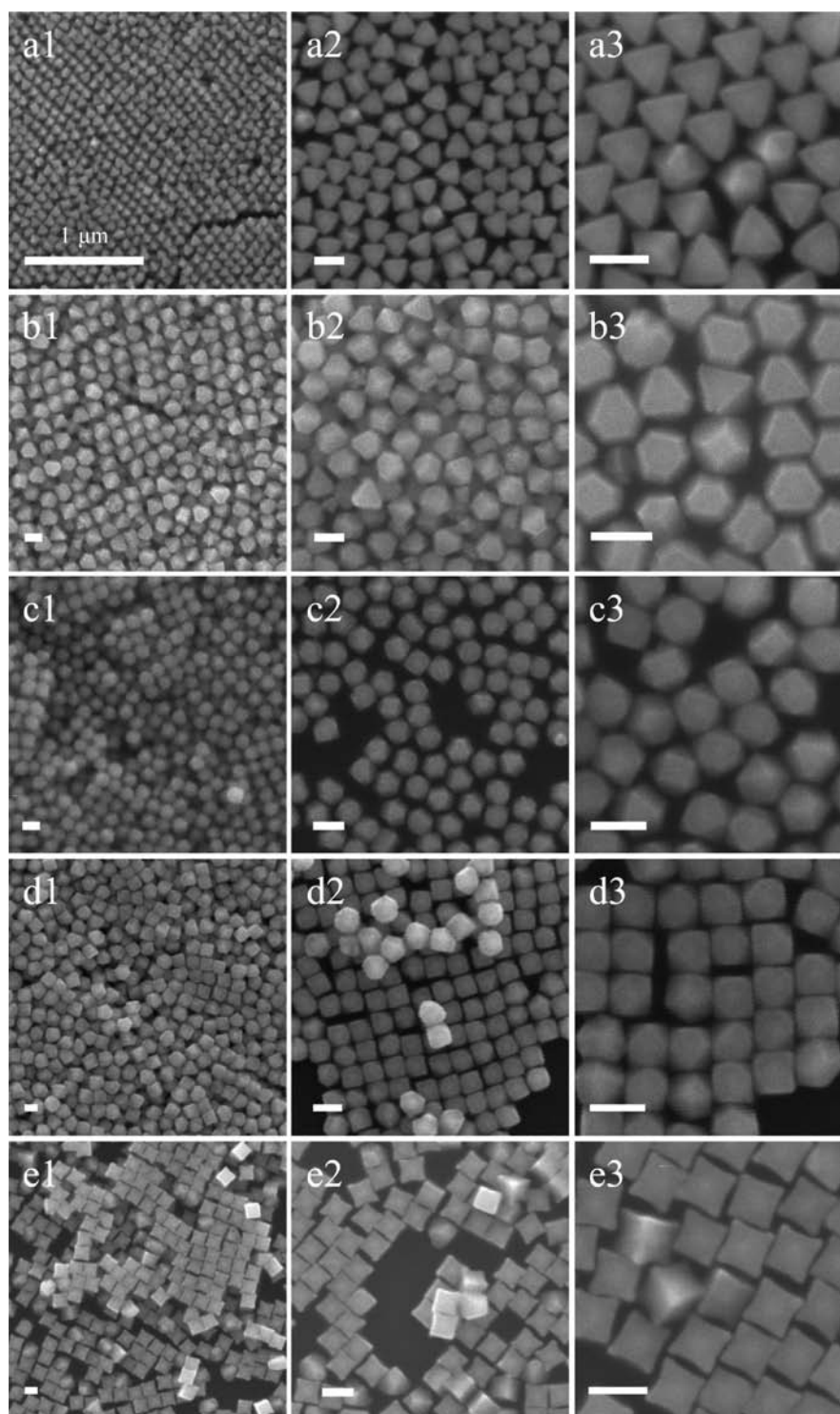


Figure 1. SEM images of the synthesized Au–Pd core–shell nanocrystals with (a1–a3) octahedral, (b1–b3) truncated octahedral, (c1–c3) cuboctahedral, (d1–d3) truncated cubic, and (e1–e3) concave cubic shapes. SEM images recorded at three different magnifications are shown for each sample. All scale bars are equal to 100 nm.

generally produced, although in some experiments the average particle sizes can vary from 42 to 56 nm (see Figure S1 in the Supporting Information). For the overgrowth of Pd shells on these octahedral gold nanocrystals, H_2PdCl_4 was added to an aqueous mixture of CTAB surfactant and the gold octahedra. The solution was subsequently stirred for 15 min for the

complete formation of the $[\text{CTA}]_2[\text{PdBr}_4]$ complex species before the addition of ascorbic acid to reduce the palladium source (see discussion later). Ligand exchange is believed to take place because the formation of $[\text{PdBr}_4]^{2-}$ is favorable. Stability of $[\text{PdBr}_4]^{2-}$ has been reported to be 10^3 – 10^4 times higher than that of $[\text{PdCl}_4]^{2-}$.²¹ This stirring time is believed to be necessary

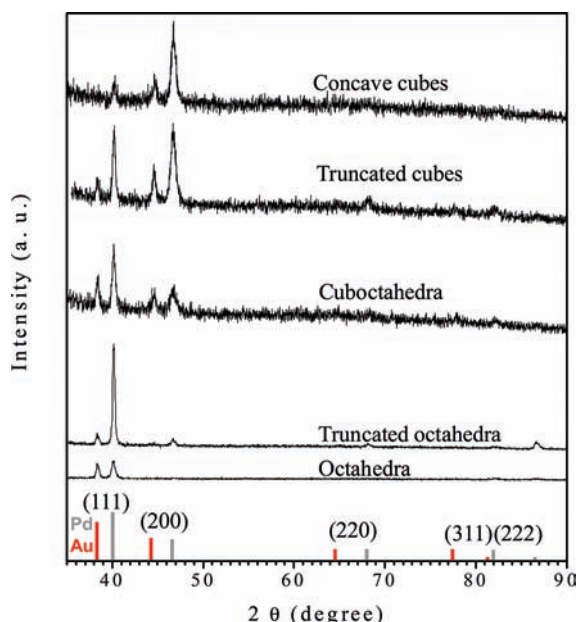


Figure 2. XRD patterns of the different Au–Pd core–shell nanocrystals synthesized. Standard XRD patterns for Au and Pd are also provided.

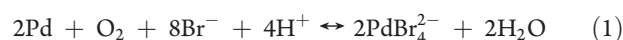
for the systematic control of shell morphology; cubic products may form without this extended stirring time. The products were collected after 12 h of reaction at 35 °C. Variation in the amount of gold nanocrystals introduced led to the formation of Au–Pd core–shell heterostructures with systematic shape evolution (see Scheme S1 for the experimental procedure).

Figure 1 gives SEM images of the synthesized Au–Pd core–shell heterostructures. By simply reducing the volume of the octahedral gold nanocrystals used from 450 μL to 400, 350, 300, and 200 μL , Au–Pd core–shell nanocrystals with octahedral, truncated octahedral, cuboctahedral, truncated cubic, and concave cubic structures were obtained, respectively. This direct growth of bimetallic core–shell nanocrystals over such a wide range of particle shape evolution is likely unprecedented. The nanocrystals are highly uniform in size and shape that they can readily form long- or short-ranged self-assembled structures. The core–shell octahedra, truncated octahedra, cuboctahedra, truncated cubes, and concave cubes have average sizes of 121, 96, 77, 68, and 79 nm, respectively (see Figure S2 and Table S1 for the particle size distribution).

The core–shell composition of these nanocrystals has been determined. Figure 2 presents the XRD patterns of the core–shell nanocrystals. Both Au and Pd show reflection peaks. Weaker peak intensities have been recorded for Au because it is located inside the particles. As expected, octahedra and truncated octahedra show dominantly strong (111) peak because of their {111} faces and preferred orientation of deposition on the substrates. The (200) peak intensities increase progressively, while the (111) peak intensities decline continuously from truncated octahedra to concave cubes as the fraction of {100} facets increases. Further structural analysis of the particles was performed through TEM characterization. Figure 3 shows TEM images, corresponding selected-area electron diffraction (SAED) patterns, and the representative drawings of individual Au–Pd core–shell concave cube, cuboctahedron, and octahedron. A cuboctahedron viewed along two different directions is displayed. Additional TEM images of the concave cubes, cuboctahedra, and

octahedra showing clear presence of the octahedral Au nanocrystal cores are available in the Supporting Information (see Figure S3). Because of the relatively thick shell thickness, their SAED patterns generally give diffraction spots of Pd. However, a Au ($\bar{2}00$) diffraction spot can be clearly seen in the SAED pattern of a cuboctahedron (see panel b2). The fact that both Au and Pd diffraction spots are aligned in the same directions indicates that the lattice orientations of Au and Pd are in exactly the same in these nanocrystals. Representative drawings of the heterostructures depict this exact orientation relationship. The core–shell composition of concave cubes was further verified by using a high-angle annular dark-field scanning TEM technique (HAADF–STEM) and an EDS analysis (see Figure S4). The core geometry can be more easily identified in the HAADF–TEM images. EDS elemental mapping and line scan images confirm the Au core and Pd shell composition.

The contour of the concave cubes immediately suggests that the surfaces of each concave cube are bounded by various high-index facets. Similar Au–Pd core–shell nanocubes with nonflat faces but slightly protruded corners have been synthesized before by growing Pd shells on octahedral Au nanocrystal cores in the presence of H_2PdCl_4 , ascorbic acid, and CTAB surfactant, but their surface facets were not examined.² A fundamental difference in our synthetic strategy is the extended stirring time to form the $[\text{CTA}]_2[\text{PdBr}_4]$ complex species first. This allows the use of variation in the volume of Au cores to achieve systematic shape evolution of final products. From their TEM images, the θ angles between the depressed faces of a projected concave nanocube and the {100} face of a perfect cube were measured. Figure 4 summarizes the distribution of the measured angles. These various θ angles show that the surfaces of the concave cubes should correspond to a number of high-index facets. Table S2 offers a list of theoretical θ angles and their corresponding surface facets. From this list, it appears that the surfaces of concave cubes are highly bounded by a combination of {410}, {510}, {610}, {720}, and {830} facets. The {830} facet has the highest measured frequency. Of course, the concave cubes may also be bounded by the {hkk} facets.²² High-resolution TEM images of a single concave cube were taken (see Figure S5). Lattice fringes with a d -spacing of 0.22 nm were measured, which should correspond to the (111) lattice planes of Pd. A close inspection of the crystal edges reveal nonsmooth, but fairly rugged surfaces with many steps. This suggests that each face of a concave cube can even be constructed of various high-index facets. The generation of these highly atomically irregular surface structures can be partly attributed to the considerably large lattice mismatch between the (111) planes of Au and Pd at 4.64%. Lattice strain should build up as shell thickness increases. To release this lattice strain, the nanocrystals may adopt some forms of structural adjustment. Formation of these high-index facets is likely the manifestation of this structural adjustment. The fact that only concave cubes appear to exhibit high-index facets may be related to the greater shell thickness at the corners of the cubes (~ 45 nm) as compared to other particle morphologies such as the core–shell octahedra (~ 25 nm). In the presence of dissolved oxygen, continuous Pd oxidation and reduction cycles may also occur and facilitate the emergence of high-index facets.^{1,2,5} The following oxidation reaction may take place:



Previously, gold nanocubes, octahedra, and rhombic dodecahedra have been used to generate Au–Pd core–shell heterostructures

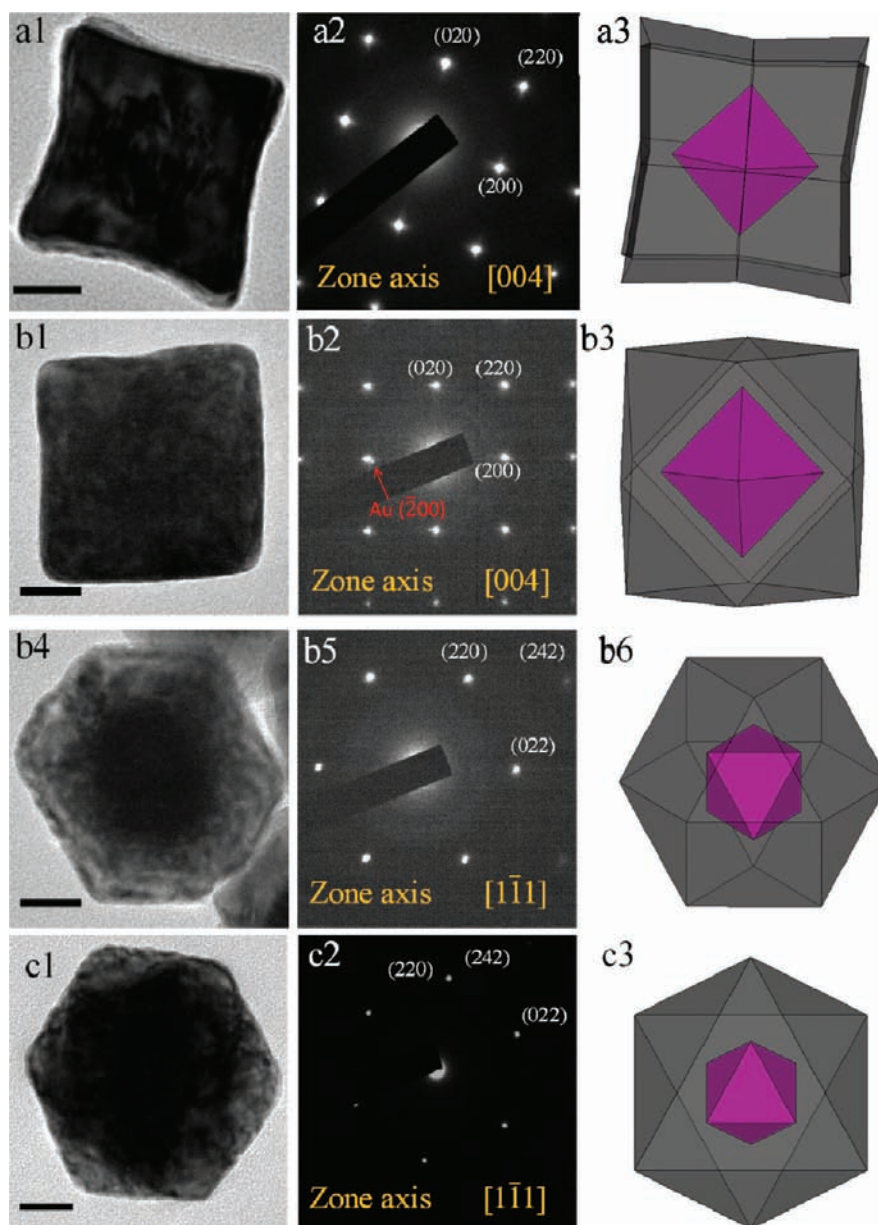


Figure 3. TEM images, corresponding SAED patterns, and representative drawings of the Au–Pd core–shell (a1–a3) concave cube, (b1–b3) cuboctahedron viewed along the $[100]$ direction, (b4–b6) cuboctahedron viewed along the $[111]$ direction, and (c1–c3) octahedron. All scale bars are equal to 100 nm.

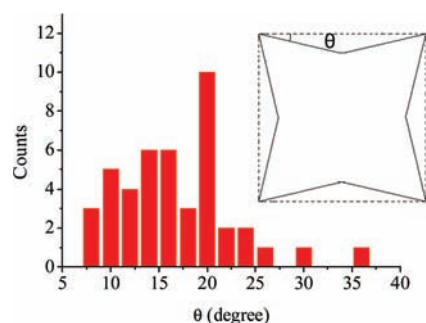


Figure 4. A plot of the θ angles measured between the depressed faces of a projected concave nanocube and the $\{100\}$ face of a perfect cube.

with a THH shell morphology bounded by high-index $\{730\}$ facets.¹ These results suggest that the effect of lattice strain can be

manifested by forming different shell structures such as concave and convex surfaces, and that interfacial stress as a function of different core geometries is less important at this particle size range. This may be related to the similar lattice mismatch percentages of the (111) , (200) , and (220) lattice planes of Pd and the corresponding planes of Au at 4.61–4.64%.¹

UV–vis absorption spectra of the various Au–Pd core–shell nanocrystals were taken (see Figure S6). All samples display a broad absorption band across the entire visible spectrum, as reflected by their gray solution color. Truncated cubes and cuboctahedra show a band maximum at ~ 400 nm. The band maxima for the concave cubes and octahedra are at ~ 460 and 530 nm, respectively. The band positions red-shift roughly with increasing particle sizes and deviation from a spherical geometry.

It is interesting to understand how variation in the amount of Au nanocrystals added to the reaction mixture affects the growth

process and leads to the systematic particle shape control. We have previously found that the control of reduction or precipitation rate is the key to the syntheses of Au, Cu₂O, and Ag₂O nanocrystals with systematic shape evolution.^{20,24–26} As mentioned earlier, extended stirring of the reaction mixture before the addition of ascorbic acid should allow the formation of the [CTA]₂[PdBr₄] complex species. This is confirmed simply by making a solution containing 1.5×10^{-2} M CTAB and 7.5×10^{-4} M H₂PdCl₄, and following the spectral changes (see Figure S7). The UV–vis absorption spectrum of H₂PdCl₄ changed significantly within seconds after the addition of CTAB, indicating a ligand exchange process has occurred to form the [CTA]₂[PdBr₄] species.^{27–29} After 12 min of reaction, a band initially appearing at 345 nm has shifted to 355 nm and is stable in its position, suggesting the reaction has been completed. The solution also becomes less transparent, implying this as a precipitate formation process. The gradual decrease in the absorbance of this band was used to monitor the growth progress in the formation of the Au–Pd core–shell nanocrystals (see Figure S8 for the spectra). Figure 5 summarizes the absorbance changes of the band at 355 nm as a function of reaction time for four core–shell nanocrystal samples examined. Interestingly, very different Pd source consumption/nanocrystal growth rates have been observed. Truncated cubes and concave cubes show the fastest reaction/growth rates, completing the growth process in 6 h. Cuboctahedra display a much slower Pd source reduction rate, and

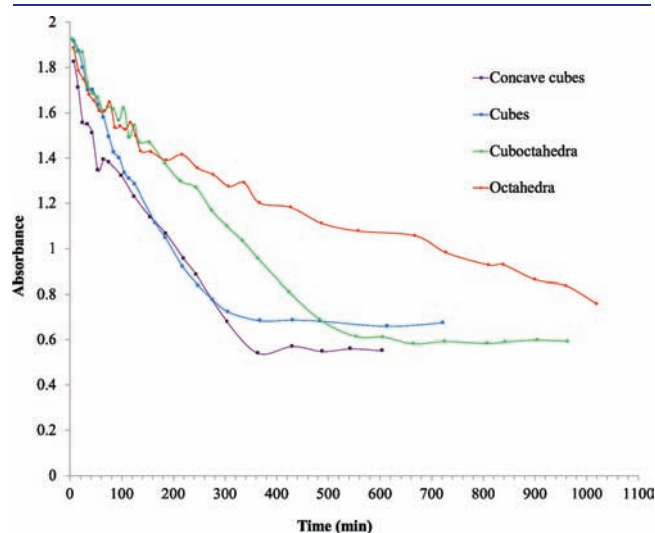


Figure 5. A plot of the absorbance changes at 355 nm versus time in the growth of various Au–Pd core–shell nanocrystals. Absorbance values eventually stop changing as the Pd source has nearly all been consumed. The final absorbance values at around 0.55–0.7 are due to the absorbance of the respective core–shell nanocrystals at 355 nm. Cubes refer to the truncated cubes.

the nanocrystal growth process takes at least 9 h to complete. The Pd source reduction rate is very slow for the formation of core–shell octahedra, and the absorbance at 355 nm continues to decline even after 17 h of reaction. The results show the widely different reduction rates yield Au–Pd core–shell nanocrystals with morphology variation. This conclusion is consistent with our previous observations in the preparation of nanocrystals with systematic shape evolution. In the synthesis of these core–shell nanocrystals, fewer amounts of octahedral gold nanocrystals were used to make concave cubes and truncated cubes. A largest volume of the gold nanocrystal solution was introduced to obtain core–shell octahedra. It is possible that the relatively large number of gold core particles completing for the same amount of Pd source and available ascorbic acid leads to a slower reaction rate and the formation of heterostructures with thinner shells. Core–shell octahedra then result. On the other hand, a faster growth rate facilitates more Pd atom deposition and the formation of heterostructures with thicker shells to produce concave cubes and truncated cubes.

Of course, the core–shell nanocrystals have already been formed long before the Pd source is completely consumed. We have examined the intermediate particles in the synthesis of core–shell truncated octahedra (see Figure S9). After 30 min of reaction, Au–Pd core–shell octahedra with sizes of ~ 50 nm have been synthesized. Corner truncation is not obvious due to the thin Pd shells. Twisted or wormlike nanostructures can be seen surrounding some smaller particles with sizes of ~ 35 nm. The twisted Pd nanostructures and the surrounding small particles of a few nanometers in size should be incorporated into the growing particles to become the shells. This mode of shell growth is reminiscent of the growth process observed in the synthesis of Au–Pd core–shell THH nanocrystals.¹ After 1 h of reaction, the truncated octahedral particle shape is clearly identifiable, although some nanocrystals still do not possess sharp facets, and their sizes are just 60–70 nm. It should take considerably more time for the particles to undergo further surface reconstruction and grow to their final dimensions with sharp facets.

It would be interesting to evaluate the catalytic activities of these core–shell nanocrystals. Concave cubes enclosed by high-index facets and octahedra bounded by {111} facets were chosen

Table 1. Comparative Reactivity of Au–Pd Core–Shell Octahedra and Concave Cubes for Catalyzing Suzuki Coupling of Iodobenzene and Phenylboronic Acid^a

reaction time	1 h	0.5 h
heterostructure morphology	octahedra	concave cubes
yield of each cycle	first	85%
	second	84%
	third	84%

^a Three cycles have been performed.

Scheme 1. Schematic Representation of the Suzuki Cross-Coupling Reactions Carried Out in This Study

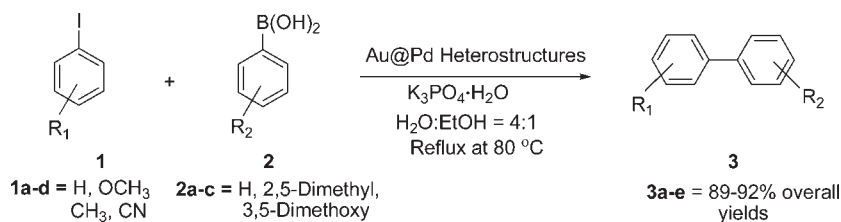
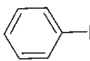
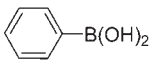
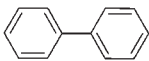
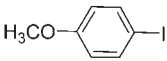
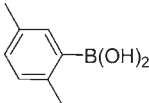
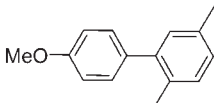
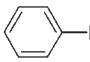
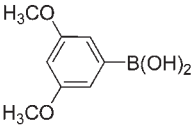
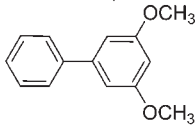
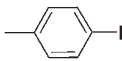
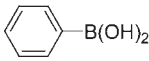
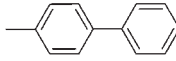
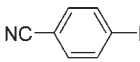
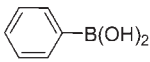
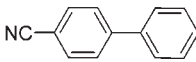


Table 2. Suzuki Coupling Reactions between Different Aryl Iodides and Arylboronic Acids Using Au–Pd Core–Shell Concave Cubes as the Catalysts

Entry	Aryl Iodide	Arylboronic Acid	Coupling Product	Isolated Yield (%) ^a
3a				91 ^b
3b				92
3c				90 ^b
3d				90 ^b
3e				89 ^b

^aDetermined on the basis of the weight of purified samples (%).

^bCompounds 3a and 3c–e were characterized by comparison of ¹H and ¹³C NMR spectra with literature data.³¹

for their comparative activity for catalyzing a Suzuki cross-coupling reaction. Figures S10 and S11 offer SEM images of the nanocrystals before and after conducting the reaction. Particle morphology remains unchanged after the reaction. The volumes of colloidal particle solutions used have been adjusted such that both samples contained nanocrystals with approximately the same total surface area. Scheme 1 gives the reaction conditions. A water/ethanol mixed solution was used as the solvent. The coupling reaction between iodobenzene and phenylboronic acid to form biphenyl was performed. To check the recyclability of these nanocrystal catalysts, three cycles of reaction were carried out using the same nanoparticles. As shown in Table 1, the concave cubes and octahedra are effective and recyclable catalysts for the Suzuki coupling reaction with product yields of 89–91% and 84–85%, respectively. However, these product yields were achieved in just 30 min for the concave cubes, but 1 h was required for the octahedra. Turnover frequency (TOF) is $\sim 2.4 \text{ s}^{-1}$ for the octahedra (see the Supporting Information for the calculations). TOF number for the concave cubes is $\sim 6.4 \text{ s}^{-1}$, assuming they are perfect cubes. If their concave shapes are considered, total surface atoms on a single nanocrystal should increase significantly, and the actual TOF number is much lower than 6.4 s^{-1} . The correct TOF number for the concave cubes should still be larger than 2.4 s^{-1} , because the product yield is only 50–60% for the octahedra after 30 min of reaction. This large reaction rate difference clearly demonstrates the superior catalytic performance of the Au–Pd core–shell concave cubes. This excellent catalytic activity is attributed to their possession of various high-index facets. Pd concave cubes bounded by high-index {730} facets have also recently been shown to exhibit a substantially better catalytic activity for a Suzuki coupling reaction than do flat Pd nanocubes.³⁰ To broaden the scope of utility of these nanocrystal catalysts, the concave cubes have been employed to catalyze a range of Suzuki coupling reactions using aryl iodides and arylboronic acids containing electron-donating

and -withdrawing substituents (see Table 2). The product purity has been confirmed by NMR spectroscopy and mass spectrometry (see the Supporting Information).³¹ Consistently excellent product yields of 89–92% have been obtained after 1 h of reaction, indicating that the concave cubes are versatile catalysts with potential for synthesizing bioactive compounds.

CONCLUSION

In this study, the direct fabrication of Au–Pd core–shell heterostructures with a progressive shell morphology evolution has been demonstrated. By simply adjusting the volume of the gold nanocrystal cores added to the reaction mixture, core–shell octahedra, truncated octahedra, cuboctahedra, truncated cubes, and concave cubes have been successfully synthesized. The core–shell particle structures have been extensively characterized. The concave cubes are bounded by various high-index facets, including the {410}, {510}, {610}, {720}, and {830} facets. Formation of the $[\text{CTA}]_2[\text{PdBr}_4]$ species has been identified. Time-dependent UV–vis absorption spectra reveal widely different reduction rates in the growth of these core–shell nanocrystals. Faster PdBr_4^{2-} consumption rates are linked to the production of truncated cubes and concave cubes, while a much slower reaction rate is associated with the generation of octahedra. Both the core–shell concave cubes and octahedra can serve as effective and recyclable catalysts for catalyzing a Suzuki coupling reaction, but the concave cubes show a much superior performance as compared to that of the octahedra with a much shorter reaction time. This excellent catalytic activity is attributed to their high-index surface facets. The concave cubes also efficiently catalyze a broad range of Suzuki coupling reactions. Thus, the method described here not only yields a variety of Au–Pd core–shell heterostructures that are synthetically challenging to prepare, but the nanocrystals can also offer enhanced catalytic activities.

■ ASSOCIATED CONTENT

S Supporting Information. Schematic drawing of the nanocrystal synthesis procedure, SEM images of the octahedral gold nanocrystal cores, particle size distribution histograms, TEM images of the core–shell nanocrystals and their intermediate structures, HAADF–STEM images of the nanocrystals, a table of angles for the high-index facets, high-resolution TEM images of a concave cube, UV–vis absorption spectra of the core–shell nanocrystals, time-dependent UV–vis spectra, and NMR spectra. This material is available free of charge via the Internet at <http://pubs.acs.org>.

■ AUTHOR INFORMATION

Corresponding Author

hyhuang@mx.nthu.edu.tw

■ ACKNOWLEDGMENT

We thank the National Science Council of Taiwan for the support of this research (Grant NSC 98-2113-M-007-005-MY3).

■ REFERENCES

- (1) Lu, C.-L.; Prasad, K. S.; Wu, H.-L.; Ho, J.-a. A.; Huang, M. H. *J. Am. Chem. Soc.* **2010**, *132*, 14546–14553.
- (2) Fan, F.-R.; Liu, D.-Y.; Wu, Y.-F.; Duan, S.; Xie, Z.-X.; Jian, Z.-Y.; Tian, Z.-Q. *J. Am. Chem. Soc.* **2008**, *130*, 6949–6951.
- (3) Habas, S. E.; Lee, H.; Radmilovic, V.; Somorjai, G. A.; Yang, P. *Nat. Mater.* **2007**, *6*, 692–697.
- (4) Cho, E. C.; Camargo, P. H. C.; Xia, Y. *Adv. Mater.* **2010**, *22*, 744–748.
- (5) (a) Tsuji, M.; Nishio, M.; Jiang, P.; Miyamae, N.; Lim, S.; Matsumoto, K.; Ueyama, D.; Tang, X.-L. *Colloids Surf., A* **2008**, *317*, 247–255. (b) Tsuji, M.; Matsuo, R.; Jiang, P.; Miyamae, N.; Ueyama, D.; Nishio, M.; Hikino, S.; Kumagae, H.; Kamarudin, K. S. N.; Tang, X.-L. *Cryst. Growth Des.* **2008**, *8*, 2528–2536.
- (6) Tsuji, M.; Yamaguchi, D.; Matsunaga, M.; Alam, Md. J. *Cryst. Growth Des.* **2010**, *10*, 5129–5135.
- (7) Tsuji, M.; Yamaguchi, D.; Matsunaga, M.; Ikedo, K. *Cryst. Growth Des.* **2011**, *11*, 1995–2005.
- (8) Wu, Y.; Jiang, P.; Jiang, M.; Wang, T.-W.; Guo, C.-F.; Xie, S.-S.; Wang, Z.-L. *Nanotechnology* **2009**, *20*, 305602.
- (9) Xiang, Y.; Wu, X.; Liu, D.; Jiang, X.; Chu, W.; Li, Z.; Ma, Y.; Zhou, W.; Xie, S. *Nano Lett.* **2006**, *6*, 2290–2294.
- (10) Wang, F.; Li, C.; Sun, L.-D.; Wu, H.; Ming, T.; Wang, J.; Yu, J. C.; Yan, C.-H. *J. Am. Chem. Soc.* **2011**, *133*, 1106–1111.
- (11) Lee, J. Y.; Yu, Y.; Zhang, Q.; Liu, B. *J. Am. Chem. Soc.* **2010**, *132*, 18258–18265.
- (12) Lee, Y. W.; Kim, M.; Kim, Z. H.; Han, S. W. *J. Am. Chem. Soc.* **2009**, *131*, 17036–17037.
- (13) Park, G.; Seo, D.; Jung, J.; Ryu, S.; Song, H. *J. Phys. Chem. C* **2011**, *115*, 9417–9423.
- (14) Ma, Y.; Li, W.; Cho, E. C.; Li, Z.; Yu, T.; Zeng, J.; Xie, Z.; Xia, Y. *ACS Nano* **2010**, *4*, 6725–6734.
- (15) Wang, A.; Peng, Q.; Li, Y. *Chem. Mater.* **2011**, *23*, 3217–3222.
- (16) DeSantis, C. J.; Peeverly, A. A.; Peters, D. G.; Skrabalak, S. E. *Nano Lett.* **2011**, *11*, 2164–2168.
- (17) Kuo, C.-H.; Hua, T.-E.; Huang, M. H. *J. Am. Chem. Soc.* **2009**, *131*, 17871–17878.
- (18) Wang, W.-C.; Lyu, L.-M.; Huang, M. H. *Chem. Mater.* **2011**, *23*, 2677–2684.
- (19) Kuo, C.-H.; Yang, Y.-C.; Gwo, S.; Huang, M. H. *J. Am. Chem. Soc.* **2011**, *133*, 1052–1057.
- (20) Chung, P.-J.; Lyu, L.-M.; Huang, M. H. *Chem.-Eur. J.* **2011**, *17*, 9746–9752.
- (21) Feldberg, S.; Klotz, P.; Newman, L. *Inorg. Chem.* **1972**, *11*, 2860–2865.
- (22) Huang, X.; Zhao, Z.; Fan, J.; Tan, Y.; Zheng, N. *J. Am. Chem. Soc.* **2011**, *133*, 4718–4721.
- (23) Chen, Y.-H.; Hung, H. H.; Huang, M. H. *J. Am. Chem. Soc.* **2009**, *131*, 9114–9121.
- (24) Kuo, C.-H.; Huang, M. H. *J. Phys. Chem. C* **2008**, *112*, 18355–18360.
- (25) Ho, J.-Y.; Huang, M. H. *J. Phys. Chem. C* **2009**, *113*, 14159–14164.
- (26) Lyu, L.-M.; Wang, W.-C.; Huang, M. H. *Chem.-Eur. J.* **2010**, *16*, 14167–14174.
- (27) Fan, F.-R.; Attia, A.; Sur, U. K.; Chen, J.-B.; Xie, Z.-X.; Li, J.-F.; Ren, B.; Tian, Z.-Q. *Cryst. Growth Des.* **2009**, *9*, 2335–2340.
- (28) Berhault, G.; Bausach, M.; Bisson, L.; Becerra, L.; Thomazeau, C.; Uzio, D. *J. Phys. Chem. C* **2007**, *111*, 5915–5925.
- (29) Veisz, B.; Király, Z. *Langmuir* **2003**, *19*, 4817–4824.
- (30) Jin, M.; Zhang, H.; Xie, Z.; Xia, Y. *Angew. Chem., Int. Ed.* **2011**, *50*, 7850–7854.
- (31) (a) Han, J.; Liu, Y.; Guo, R. *J. Am. Chem. Soc.* **2009**, *131*, 2060–2061. (b) Ackermann, L.; Gschrei, C. J.; Althammer, A.; Riederer, M. *Chem. Commun.* **2006**, 1419–1421. (c) Worm-Leonhard, K.; Meldal, M. *Eur. J. Org. Chem.* **2008**, 5244–5253. (d) Castanet, A. S.; Colobert, F.; Desmurs, J. R.; Schlama, T. *J. Mol. Catal.* **2002**, *182*, 482–487.